

## **The Convective Cold Top and Quasi Equilibrium**

Christopher E. Holloway

*Department of Atmospheric and Oceanic Sciences, University of California, Los Angeles, Los Angeles, California (chollow@ucla.edu)*

J. David Neelin\*

*Department of Atmospheric and Oceanic Sciences and Institute of Geophysics and Planetary Physics, University of California, Los Angeles, Los Angeles, California*

### ABSTRACT

To investigate dominant vertical structures of observed temperature perturbations, and to test the temperature implications of the convective quasi-equilibrium hypothesis, the relationship of the tropical temperature profile to the average free tropospheric temperature is examined in Atmospheric Infrared Sounder (AIRS) satellite data, radiosonde observations, and National Centers for Environmental Prediction/National Center for Atmospheric Research (NCEP/NCAR) reanalysis. The spatial scales analyzed extend from the entire tropics down to a single reanalysis grid point or radiosonde station, with monthly to daily time scales. There is very high vertical coherence of free tropospheric temperature perturbations. There is also fairly good agreement throughout the free troposphere between observations and a theoretical quasi-equilibrium perturbation profile calculated from a distribution of moist adiabats. The boundary layer is fairly independent from the free troposphere, especially for smaller scales.

A third vertical feature of the temperature perturbation profile is here termed the "convective cold top:" a robust negative correlation between temperature perturbations of the vertically averaged free troposphere and those of the upper troposphere and lower stratosphere. The convective cold top is found for observations and reanalysis at many temporal and spatial scales. Given this prevalence, the literature is reviewed for previous examples of what is likely a single phenomenon. One simple explanation is proposed: hydrostatic pressure gradients from tropospheric warming extend above the heating, forcing ascent and adiabatic cooling. The negative temperature anomalies thus created are necessary for anomalous pressure gradients to diminish with height.

### 1. Introduction

This study addresses the typical vertical structure of temperature perturbations in the tropical atmosphere. Assumptions regarding the effects of deep convection on temperature structure are implicit in most large-scale tropical models. More specifically, convective parameterizations being used in current climate models typically involve the consumption of buoyancy and an explicit or implicit relaxation toward a neutral reference profile. Commonly, this reference profile is related to a moist adiabat originating from a parcel in the atmospheric boundary layer. The idea that convection consumes vertical instability, such as convective available potential energy (CAPE), at roughly the rate that it is created by large-scale forcing, is generally called quasi-equilibrium (QE) theory and is clearly presented in Arakawa and Schubert (1974); it can also be found in various forms in Manabe et al. (1965), Betts

(1973), Betts and Miller (1986), Emanuel (1991), Moorthi and Suarez (1992), Randall and Pan (1993), Zhang and McFarlane (1995), and Raymond (1997).

One application of QE theory involves simplifying temperature and moisture structure in the vertical for use in intermediate complexity models, such as the quasi-equilibrium tropical circulation model (QTCM) (Neelin, 1997; Neelin and Zeng, 2000). The main assumption made by such a model is that most of the tropospheric variance can be represented by coherent vertical structures for temperature and moisture which in turn lead to simplified prediction of baroclinic pressure gradients and precipitation, respectively. To calculate baroclinic pressure gradients and resulting velocity fields, the shape of the vertical temperature structures is important.

This study tests both the ability to represent vertical temperature structure in a simplified manner and the adherence to a moist-adiabatic perturbation profile as predicted by QE. Note that these are two separate questions, although there is evidence that QE should have an important constraining effect in the tropics (Arakawa 2004).

\*Corresponding author address: J. David Neelin, Department of Atmospheric and Oceanic Sciences, University of California, Los Angeles, 405 Hilgard Avenue, Los Angeles, CA 90095-1565.  
E-mail: neelin@atmos.ucla.edu

Several studies have used observations to determine whether and to what degree quasi-equilibrium holds. Xu and Emanuel (1989) found that soundings over the western Pacific were nearly neutral to moist adiabats lifted from the upper boundary layer. Brown and Bretherton (1997) found significant correlations between vertical mean temperatures in the troposphere and boundary layer equivalent potential temperature ( $\theta_e$ ), but the constants of proportionality were about half of those predicted by strict QE. Sobel et al. (2004) found fairly large correlations between boundary layer and lower tropospheric temperatures but lower correlations with upper tropospheric temperatures. One challenge faced by all of these studies is exactly which boundary layer parcel, in terms of horizontal and vertical location, to choose when making comparisons to free tropospheric observations. Another challenge is the relatively sparse data available over the tropical oceans.

The present study largely sidesteps the first challenge by regressing temperature perturbations at each level on the vertically averaged free tropospheric perturbations, and comparing these with corresponding regressions calculated from a range of moist adiabats. This makes the comparisons less sensitive to the specific moist adiabat used, and thus to the specific boundary layer conditions measured locally. We also investigate the degree of vertical coherence of perturbations independent of the particular shape found. Radiosondes, Atmospheric Infrared Sounder (AIRS) satellite data, and National Centers for Environmental Prediction/National Center for Atmospheric Research reanalysis (NCEP hereafter) are used to maximize the range of time and space scales. A highly coherent free troposphere at all scales and for all datasets is found, with reasonably moist-adiabatic regression curve shapes.

One result not expected from simple QE theory, discussed in section 5, is the significant and robust *negative* correlation between temperature perturbations near and above the tropopause and those of the vertically averaged free troposphere. We refer to this phenomenon here as the "convective cold top," although this assumes that on the analyzed time scales perturbations of vertically averaged free tropospheric temperature are directly related to deep convection. Given the prevalence with which we encounter this feature, it is not surprising that many previous publications contain instances of what appear to be, in retrospect, similar phenomena. Section 5a is a brief review of the relevant literature. We argue that one simple explanation can explain why this result is so prevalent. We show that even in a simple linear model in hydrostatic balance broad ascent and thus adiabatic cooling occur slightly above the maximum extent of the convective heating. Negative temperature anomalies

are required by simple dynamical constraints. In addition to addressing the coherent free tropospheric temperature structure and the convective cold top, we note the relative independence of the boundary layer, although this is not our main focus.

Section 2 is a description of the data used in this study, followed by the data analysis method in section 3 and analysis results in section 4. Section 5 discusses the convective cold top in relevant literature and in a simple model, and expands our explanation for it. A summary follows in section 6.

## 2. Observations and Data

### *a. AIRS satellite data*

We use Level 2 version 4 AIRS satellite data soundings averaged over horizontal boxes within 15°S–15°N at standard pressure levels (1000, 925, 850, 700, 600, 500, 400, 300, 250, 200, 150, 100, 70, 50, 30, 20, 15, and 10 hPa). Each footprint has 45 by 45 km horizontal resolution. The AIRS instrument is aboard the polar orbiting Aqua satellite and combines microwave passive radiation with infrared radiation, allowing for more accurate vertical representations of temperature and moisture. Daily values have been found by averaging twice-daily swath profiles which fall in each box in a given 24-hour period. Only the highest quality (total profile flag = 0) soundings have been retained, meaning mainly those over the ocean and outside of heavily clouded regions (see Susskind et al. 2003). The temperature data at this quality level have rms differences of 1 K or less in the free troposphere, around 1 K near the surface, and around 2 K or less in the lower stratosphere, when compared to collocated and coincident radiosondes, with biases of 0.2 K or less at most levels and up to 0.8 K above the tropopause (Divakarla et al. 2006, Tobin et al. 2006).

The daily time scale data range over the two years from 19 November 2003 to 18 November 2005, with two missing days. The first three harmonics of the seasonal cycle and an independent two-year harmonic (to account for the quasi-biennial oscillation, or QBO) have been removed (see section 3). For the smallest spatial scale over half the days were missing, so that the next largest spatial scale data (10°S–10°N, 140°E–180°E) was used on missing days only for purposes of finding harmonics. The monthly time scale was found by averaging the anomalies into 24 monthly values.

### *b. CSU TOGA COARE gridded rawinsonde data*

The Colorado State University (CSU) sounding data (Ciesielski et al. 2003) come from four months of

the Tropical Ocean Global Atmosphere Coupled Ocean Atmosphere Response Experiment (TOGA COARE) dataset, provided by the R. Johnson research group. These months are during the Intensive Observing Period (IOP), November 1992–February 1993. The source data are from a merged profiler/rawinsonde dataset (Ciesielski et al. 1997) and sounding data from other Priority Sounding Sites (PSS). These temperature and moisture data are available on a horizontal  $1^\circ$  by  $1^\circ$  latitude/longitude grid at 25 hPa vertical resolution. They have been analyzed at standard pressure levels (as in AIRS, except above 150 hPa there are levels every 25 hPa up to 25 hPa), and the four times daily analyses have been averaged into daily values.

#### *c. CARDS radiosonde data*

Three stations on Pacific warm pool islands have been selected from the Comprehensive Aerological Reference Data Set (CARDS) (Eskridge et al. 1995) because of their locations and their almost 50 shared years of observations (1953–1999). The three stations are Koror ( $7.3^\circ\text{N}$ ,  $134.5^\circ\text{E}$ ), Chuuk ( $7.5^\circ\text{N}$ ,  $151.8^\circ\text{E}$ ), and Majuro Atoll ( $7.1^\circ\text{N}$ ,  $171.4^\circ\text{E}$ ). The CARDS data have 50 hPa vertical resolution between 1000 and 100 hPa, and then include 70, 50, and 30 hPa levels above, and have been subjected to a rigorous quality control process by the data team (Eskridge et al. 1995). We have averaged all available daily data into monthly values and then removed the seasonal cycle. The much smaller sample size for pressure levels above 250 hPa (around 85 months, almost all at the very end of the larger time series) made it necessary to slightly adjust the domain of the vertical average being used in our regressions for CARDS data (and the accompanying moist-adiabatic slope curve) from 850–200 hPa to 850–250 hPa. Note that the CARDS dataset has now been superseded by the Integrated Global Radiosonde Archive, although for the purposes of this study there are no major differences (Durre et al. 2006).

#### *d. NCEP/NCAR reanalysis*

The NCEP reanalysis (Kalnay et al. 1996) consists of model initialization data with assimilated observations that have been analyzed with a GCM in a consistent manner over many years. Temperature data are located on a  $2.5^\circ$  by  $2.5^\circ$  horizontal grid at standard pressure levels (as in AIRS, except without the 15 hPa level). The years 1979–2003 are used because of better data quality in the satellite era. Monthly anomalies are taken for the entire period to remove the seasonal cycle. Daily data have been used for the same two years as the AIRS data, with the same harmonics removed, for

comparison purposes. For monthly anomalies, we have removed the four months of the Intensive Observing Period (IOP) of TOGA COARE, November 1992–February 1993, because of problems during those four months with the assimilation of TOGA COARE data leading to significant temperature outliers in the Pacific warm pool region. NCEP is a useful proxy for QE-type behavior, since it assimilates real data but relies on a large-scale numerical assimilation model which in turn uses a relaxed Arakawa-Schubert convective parameterization with a quasi-equilibrium closure that for deep convection relies on a moist adiabat-like test of CAPE, accounting for entrainment, for boundary layer parcels (Pan and Wu 1995).

#### *e. Analysis regions*

To compare several different sources of data at many spatial scales in the tropics, we have defined a few main horizontal boxes for our analyses. We focus on tropical regions, centering our smaller boxes over the Pacific warm pool, an area of active convection where TOGA COARE data was available. We also analyze one largely non-convecting region of the eastern tropical Pacific.

The exact boundaries of these boxes differ slightly with each dataset. For instance, the latitude/longitude boundaries listed for NCEP refer to the grid points used, so that the actual range covered extends  $1.25^\circ$  beyond the stated range. Similarly, the range covered by the CSU TOGA COARE gridded dataset extends  $0.5^\circ$  beyond the stated range. The boundaries in the case of AIRS data refer to the centers of footprints included (and each footprint is 45 km wide). AIRS data is also only over oceans and a few large lakes, and outside regions with high cloud liquid water, as discussed above. The CARDS data used are an average of three radiosonde stations on Pacific islands on or near the line  $7^\circ\text{N}$ ,  $135^\circ\text{E}$ – $170^\circ\text{E}$ , so we use that label on CARDS plots.

### **3. Method of Analysis**

This analysis tests the coherence of temperature perturbations in the vertical with an emphasis on the free troposphere, where relatively fast-moving gravity waves caused by deep convection are assumed to spread uniform temperature signals over large regions in short amounts of time (on the order of one hour over 100 km, Nicholls et al. 1991). At each pressure level, temperatures have been regressed on free tropospheric column average temperatures and the linear regression coefficient (slope) has been plotted. This approach is related to that used in Fig. 3 of Chiang and Sobel

(2002), which shows regressions on monthly anomalies of NCEP temperatures (from 800 to 5 hPa) of the first principle component of the same temperature perturbations from 750–200 hPa. The first principle component in that study had a 0.95 linear correlation coefficient with the same time series of microwave sounding unit (MSU) channel 2 tropospheric temperature, a measure of vertical average temperature.

For comparison to the regression analysis on the temperature data, the corresponding analysis has been done for a distribution of reversible moist adiabats (neglecting ice). Note that although we refer to these profiles as moist adiabats, they begin along a dry adiabat until reaching the lifting condensation level (LCL), which occurs between 925 and 900 hPa. First, 60 evenly-spaced parcels are given a range of temperatures at 1000 hPa, starting with constant relative humidity. For the cases presented in this article, all moist-adiabatic slope curves come from the same temperature range (298–301 K) and the same relative humidity (83%) at 1000 hPa. These values are typical of warm tropical regions under precipitating conditions, as discussed in the Appendix. A sensitivity analysis using the daily NCEP 1000 hPa data, also described in the Appendix, found very little variability in tropical tropospheric regression coefficients. The code for calculating the moist adiabats comes from a script included with Emanuel (1994). These slopes could alternatively have been calculated analytically using a moist-adiabatic equation linearized around a specific moist adiabat. However, we chose the current method because it works just as well, more exactly parallels our data analysis method, and allows us to use ranges of values to make a linear approximation across the nonlinear range (though admittedly the linearization made from the moist adiabat at the center of the range is virtually indistinguishable from our result). This moist-adiabatic perturbation profile lines up closely with the temperature perturbation profile used for the QTCM based on an analytical linearization around the equation for a moist pseudoadiabat (Neelin and Zeng 2000).

At daily time scales for NCEP and AIRS we removed the first two-year harmonic, since it is independent of the three seasonal cycle harmonics removed and since the QBO cycle over the particular two years analyzed seems to be fairly close to a two-year period, based on NOAA Climate Prediction Center data. The variability associated with this harmonic is small in the troposphere, but significant above the tropopause, and it is clearly of much larger time scale than those of interest for daily data. We did not remove any QBO-related cycle from the longer time series because of difficulties in characterizing a quasi-periodic phenomenon, although this would be useful future work.

Figure 1 shows an example of a scatterplot used to determine one linear regression coefficient (slope). The y-axis is the temperature anomaly at a given pressure level (in this case 400 hPa), while the x-axis is the free tropospheric average temperature anomaly between 850 and 200 hPa. Each point represents a single time (day in this example) averaged over the spatial box shown. The slope of the linear regression line is the value that will appear in later figures. The dashed grey line represents the same regression using a series of moist adiabats, shifted in position for clarity (the scatterplot is not shown but is almost indistinguishable from a straight line, with a correlation coefficient of one). Note that all moist-adiabatic slopes shown in the following figures are the same; they do not depend in this study on spatial or temporal considerations.

Our plots of correlation coefficients include grey shading between the positive and negative critical values of statistical significance at the 95% level. To account for autocorrelation, we calculate the critical value using Student’s t-test, but with the effective sample size in place of the actual sample size:

$$N_{eff} = N \frac{(1 - r_1 r_2)}{(1 + r_1 r_2)},$$

where  $N_{eff}$  is the effective sample size,  $N$  is the original sample size, and  $r_1$  and  $r_2$  are the lag-1 autocorrelations of the two time series (Bretherton et al. 1999). Differences between adjacent critical values of less than 0.05 are rounded upward for clarity, provided that the rounded values are not close to the actual data points at their respective levels. Although the correlation coefficients within the free troposphere will be slightly inflated using our method, since temperatures at those levels are also included in the vertical average, tests using vertical averages excluding the actual level in each regression show only about 1–2% differences for all but the two outermost levels, and differences in correlation coefficients of around 0.01, with a maximum difference of 0.03, again at the outermost levels.

Unlike Brown and Bretherton (1997), we do not include regressions made by reversing our dependent and independent variables. Since the vertical average temperature incorporates many relatively independent temperature observations, it should generally have less noise than the temperature at any given level. Therefore, to minimize regression error, the vertical average is more suitable as an independent variable.

## 4. Vertical structure across scales

### *a. Comparison across spatial scales*

Figure 2a shows linear regression coefficients for temperature at each pressure level regressed on free tropospheric vertically averaged temperature for two years of NCEP daily anomalies at four spatial scales, ordered from largest to smallest, along with the moist-adiabatic regressions discussed in section 3. One simple interpretation of the regression coefficients is that each value represents the change of temperature at a single level associated with a 1 K increase of free tropospheric temperature. To illustrate, the slope in Fig. 1 appears as a single point at 400 hPa in the first panel of Fig. 2a, and the moist-adiabatic slope in Fig. 1 appears as the point on the grey line at 400 hPa in every panel of Fig. 2a. The correlation coefficient for Fig. 1 likewise appears in the first panel of Fig. 2b.

We present the NCEP data first to calibrate our analysis using a dataset that should be constrained by a version of QE when and where there is deep convection (see section 2d). It is expected that NCEP, when compared with pure observations, should have higher correlations reaching even into the boundary layer and closer agreement with the moist-adiabatic curve. Below the LCL, even a strict QE parameterization will have departures from the moist-adiabatic curve since these are only temperature regressions, neglecting the degree of freedom introduced by variable relative humidity.

The values in Fig. 2a agree surprisingly well with the moist-adiabatic curve in the troposphere, especially in the free troposphere from 700 to 250 hPa. This middle layer also consistently has the highest correlation coefficients as seen in Fig. 2b, especially in the largest regions. The large correlation coefficients in the free troposphere may be partly expected because the quantity being regressed on is simply the free tropospheric vertical average (see section 3), but there is still obviously a high level of coherence among different levels within this layer, and there would be no purely statistical reason to expect the particular regression coefficients to line up with the moist-adiabatic ones. Also, the free tropospheric average used in the regressions includes 850 hPa, which nevertheless has correlation coefficients and regression coefficients typical of the boundary layer. In fact, repeating the regression analysis using the full tropospheric vertical average, or alternatively the 400 or 500 hPa temperature only, in place of the free tropospheric average does not significantly change this agreement in the free troposphere or the features present at other levels.

Above the troposphere, there are always large negative regression and correlation coefficients at some level or levels: the convective cold top. This is clearly a departure from the moist-adiabatic curve, which is positive at every level. Adherence to that curve is not expected to be as strong at levels that deep convective elements seldom reach, but the negative values clearly require explanation. The negative regression coefficients making up the convective cold top in Fig. 2a are larger for the smallest regions (although this is not true for the AIRS data).

There is a significant departure from the moist-adiabatic regressions in the “boundary layer” (which we use hereafter for 1000–850 hPa), with generally lower correlation coefficients as well. Possible reasons for this departure are discussed above and in section 6. The boundary layer in general has slightly higher correlations at larger scales.

Figure 3 shows the same regions (but only over oceans) and years as Fig. 2 (including the smallest region, since one reanalysis grid point covers 2.5° by 2.5°), but using daily anomalies of AIRS data. The three main vertical features mentioned above are very distinct. The free troposphere is well-correlated with its vertical average. The regression slopes are less in agreement with the moist-adiabatic curve in Fig. 3a than in Fig. 2a. In particular, there is a noticeable positive bulge in the middle troposphere which we have noticed in other datasets as well. This may be related to regions and places that are not precipitating as much, since an analysis using precipitation masking with NCEP reanalysis (not shown) revealed this feature to be much more pronounced during days with low precipitation. The largest AIRS region in Fig. 3a appears less moist-adiabatic than the second-largest (warmer ocean) region, probably because the largest region includes the less-convecting eastern Pacific (see section 4c). The cold top regressions and significant negative correlation coefficients in Fig. 3 are fairly consistent across regions, unlike Fig. 2.

As expected, the boundary layer has lower correlation coefficients than the free troposphere. This is more pronounced than in Fig. 2, and does not have an obvious dependence on scale. This fact may be exaggerated by our use of only the best quality AIRS profiles, which exclude deep convection and therefore are weighted toward soundings with less precipitation and less QE constraint. The larger the region, the more significant this effect, since temperatures are not as uniform for a given day (despite the tendency of gravity waves to spread temperature uniformly).

Figures 4a–b show analysis of 47 years of CARDS radiosonde monthly anomalies from three West Pacific warm pool islands averaged together. Figures made from each of the islands individually (not shown) are very similar to the average and to each other. Slopes

generally follow the moist-adiabatic curve, although they are noticeably lower in the boundary layer and higher in the lower free troposphere. Correlation coefficients are very high (almost one) in the free troposphere, becoming noticeably lower below 800 hPa. Also, there is a statistically significant cold top above the troposphere. Note that the column average temperature being regressed upon for the CARDS data and corresponding moist-adiabatic curve is a slightly smaller layer of the free troposphere (850–250 hPa) because of much smaller samples of good-quality data above 250 hPa (see section 2c).

To compare CARDS data with AIRS data, we have averaged the two years of daily anomalies used to make Fig. 3 into monthly anomalies over a region similar to, though somewhat larger than, that containing the three CARDS islands. We used this larger size region to ensure that every day had high-quality AIRS profiles. The resulting regression coefficients in Fig. 4c are even closer to the moist-adiabatic curve than the CARDS data, though they are admittedly over ocean, not islands, and for a much smaller time period, which may result in sampling issues. The cold top regression and correlation coefficients for AIRS data (Figs. 4c–d) are much larger in amplitude than the corresponding CARDS values in Figs. 4a–b, possibly because of the relatively sparse CARDS data at high levels.

Figure 4 makes an interesting comparison with Fig. 5, which shows monthly anomalies of 25 years of NCEP reanalysis over the same four regions as Figs. 2–3. The third panel of Fig. 5a, and its associated correlation coefficients in Fig. 5b, is from a similar warm pool region and has the same main features as the observational analyses in Fig. 4. The slopes are generally closer to the moist-adiabatic curve for NCEP, though not much closer than AIRS. Going from larger to smaller scales in Fig. 5, the boundary layer becomes more independent, and there is also a slightly less coherent lower free troposphere than upper free troposphere. The convective cold top is present for all regions, though not as large or significant as in Figs. 4c–d, and not significant at the 95% level at largest scales in Fig. 5. The QBO is a very large signal in the tropical stratosphere on long time scales (Plumb and Bell 1982, Huesmann and Hitchman 2001), making it difficult to separate from a possible convective signal and also reducing statistical significance given the autocorrelations associated with the QBO.

#### *b. Comparison across time scales and sampling issues*

Since it spans many different scales, we employ the NCEP reanalysis for a direct comparison over different time scales at various regions. Comparing the monthly anomalies in Fig. 5 with the daily anomalies in Fig. 2,

the most obvious difference is that the convective cold top is larger (in both regression and correlation coefficients) for the daily time scale, particularly at smaller spatial scales, although the AIRS data in Fig. 3 do not show this dependence. In the troposphere, as expected, correlation coefficients are generally higher at all vertical levels for monthly anomalies. This agrees with a recent analysis of the tropical vertical temperature structure of European Centre for Medium-Range Weather Forecasts (ECMWF) Re-Analysis (ERA-40) monthly anomalies, which shows large tropospheric vertical coherence mainly related to El Niño Southern Oscillation (ENSO) variability, as well as an accompanying cold top feature centered from 50 to 70 hPa (Trenberth and Smith 2006). The regression coefficients line up extremely well with the moist-adiabatic curve, even at the boundary layer and at all scales (with a slight deviation at the Pacific warm pool), suggesting as expected that QE dominates temperature perturbations on longer time scales even more so than on daily time scales in the NCEP reanalysis.

We now cautiously extend our time scale comparisons to radiosonde datasets, at different locations in the Pacific warm pool region. Figure 6 shows analysis over this region for four months of daily average gridded CSU TOGA COARE merged profiler/rawinsonde data. This figure confirms a coherent free troposphere feature resembling the moist-adiabatic curve even at daily time scales. Also present are a pronounced cold top regression amplitude (significant at around the 75% level) and an independent boundary layer. Since the CARDS analysis in Figs. 4a–b, over three Pacific warm pool islands with larger time scale and a longer time series, shows extremely high correlation coefficients throughout the free troposphere, fairly low but still statistically significant correlations and slopes in the boundary layer, and a moderately significant, smaller cold top slope above, we can conjecture that our main conclusions about time scales made above with respect to NCEP also hold for radiosonde data. Note that the AIRS data in Fig. 3 also show many of the attributes mentioned above for daily time scales. Monthly AIRS anomalies analyzed over the same regions (not shown) as those in Fig. 3, however, do not differ appreciably from the daily analyses; a longer time series would help resolve this.

To interpret Fig. 6, a relatively short daily time series with the seasonal cycle still included, we made comparisons of some similar time series using NCEP reanalysis (not shown). Removing the seasonal cycle improves significance of correlation coefficients, and results in slightly more tropospheric agreement with the moist-adiabatic curve. The particular four-month period can make a significant difference in the locations of kinks in the curve, and to boundary layer

independence, which sometimes approaches the degree seen in Fig. 6 even in the reanalysis.

### *c. A non-convecting region*

As an example of a non-convecting region, we consider the eastern Pacific, from the equator to 15°S, where there is climatological annual mean subsidence at 500 hPa (as measured from the NCEP data). For monthly NCEP data, Figs. 7a–b show regression coefficients close to the moist-adiabatic curve in the free troposphere, similar to Fig. 5. One difference is that boundary layer regressions are larger, possibly because long time scale SST changes in this region are of larger amplitude than, but fairly well-correlated to, non-local tropical convective warming affecting the free troposphere. The cold top feature, as in Fig. 5a, is small and not statistically significant.

At daily scales, Figs. 7c–d show an analysis of the AIRS and NCEP data over the same region. There is clearly less agreement with the moist-adiabatic curve in Fig. 7c, especially for the AIRS data. We interpret the conformance to the moist-adiabatic curve in monthly, but not in daily, data as being due to the horizontal adjustment process by wave dynamics. We suspect that deviations from the moist-adiabatic curve in previous figures, specifically positive deviations in the middle free troposphere and negative ones in the upper free troposphere, are related to non-convecting times and places contributing to those averages. There is also less coherence in the free troposphere in Fig. 7d, and the boundary layer correlations are especially low. The cold top feature remains robust at daily scales, suggesting that the shape of the tropospheric warming, and its source (in this case, likely wave dynamics spreading temperature perturbation signals from neighboring tropical regions) is not crucially important in determining the convective cold top.

## **5. The convective cold top**

Figures 2–7 all exhibit a robust negative slope and correlation between the upper-tropospheric/lower-stratospheric temperature and the free tropospheric average temperature. In nearly all cases, at all scales, this correlation is statistically significant at the 95% level or higher, except for NCEP at monthly scales over the largest tropical spatial scales, and for a four-month raw time series of daily radiosonde data. Given the prevalence with which we find this phenomenon in our results, it is not surprising that an extensive search through the literature has uncovered many descriptions of this type of behavior in various forms, which we believe are all connected to a single underlying

mechanism. We include here a brief review of some relevant articles as well as evidence of the convective cold top in a linear Boussinesq 2D model of a uniformly-stratified fluid with prescribed heating and a semi-infinite domain. We then present a simple explanation that the cooling results from hydrostatic horizontal pressure gradients which extend above the top of the convective heating, causing divergence and broad adiabatic ascent.

### *a. Relevant studies*

Early studies of tropical cyclones noted a pool of cold air above the warm central core and hypothesized that this was due to overshooting of cumulus towers (Arakawa 1950, Koteswaram 1967). Jordan (1960) presented radiosonde observations over islands in the Pacific warm pool and suggested that very cold tropopause temperatures might be related to increased periods of deep convection. Johnson and Kriete (1982) noted observations of cold anomalies at the top of mesoscale anvils in the Indonesian region during the International Winter Monsoon Experiment (Winter MONEX) and discussed several possible reasons for this. One hypothetical cause was cloud-top radiative cooling, and evidence supporting this idea included observations by Webster and Stevens (1980), who found significant radiative cooling at cloud top which they defined as approximately 200 hPa. However, as Johnson and Kriete (1982) pointed out, the observed radiative cooling occurs in the upper layers of the clouds themselves, which according to aircraft radar data were no higher than 100 hPa, whereas the maximum cooling occurred about 1–2 km above these anvil tops. They also raised the possibility that ice injected into the lower stratosphere might create radiative cooling there, as well as the theory (by then mentioned in several places) that overshooting updrafts in convective towers could be responsible. More recent observations of cold anomalies above short time scale equatorial waves include those by Haertel and Kiladis (2004), while Reid and Gage (1996) found negative temperature correlations with the free troposphere at high levels over Truk in the western Pacific using 8 years of radiosondes.

Similar observations of mesoscale cold pools above midlatitude summertime convective complexes prompted Fritsch and Brown (1982) to perform numerical experiments using a primitive equation model with 20 km horizontal resolution. They found that a mesoscale cold pool was formed aloft in two almost identical experiments, one in which the detrainment of directly overshooting parcels was parameterized at cloud top, and the other with this direct cooling omitted. In fact, in the latter case the

broad adiabatic ascent which led to all of the cooling in that experiment was stronger than in the case where diabatic cooling was parameterized. Pandya and Durran (1996) used a fully compressible, nonhydrostatic, dry model to show that adiabatic lifting due to gravity waves above and behind squall lines can cause large negative temperature perturbations without overshooting turrets. Reid et al. (1989) and Reid (1994) correlated temperatures from radiosonde stations at various levels with the ENSO index, proposing vertical ascent and adiabatic cooling as an important possible mechanism for negative correlations at high levels. Reid (1994) also argued that, assuming a ‘‘capping level’’ above which ENSO deep convection signals are no longer projected onto geopotential gradients, there must be cooling above tropospheric heating. This argument, applied to more varied scales, is similar to our overall explanation for why the convective cold top is so prevalent. The idea that adiabatic ascent might vary depending on the amount of concurrent diabatic cooling will also be discussed in more detail below.

Highwood and Hoskins (1998) presented several mechanisms by which deep convection might influence the cold point tropopause. They showed that a Gill-type model (Gill 1980) with prescribed heating generates large-scale adiabatic cooling at high levels associated with equatorial Kelvin and Rossby waves. They also discussed downward control via the stratospheric pump (i.e., midlatitude cyclones generate breaking waves in the stratosphere, causing divergence and adiabatic cooling over the tropics and leading to enhanced deep convection), and the possible contribution of overshooting turrets (e.g. as observed on small scales by Danielsen 1993). Teitelbaum et al. (2000) also discussed these possible mechanisms for stratospheric cooling related to convection.

On long time scales, some authors have proposed that deep convection could be related to the QBO in the stratosphere via several mechanisms, including dynamical cooling of the tropopause layer by the east phase of the QBO, although observations show that that phase does not always accompany cooling (e.g. Collimore et al. 2003). Kuang and Bretherton (2004) argued that cooling at the cold point tropopause (and hence the drying of air entering the stratosphere) is strongly tied to convection, mainly through turbulent mixing (overshooting parcels), contradicting several other studies advocating a more gradual process largely related to radiative effects (e.g. Holton and Gettelman 2001, Thuburn and Craig 2002). Kuang and Bretherton (2004) used a cloud-resolving model (CRM) with continuously active convection, but they could not address the question as to whether turbulence or broad adiabatic ascent is more important, since convectively driven adiabatic ascent would also be correlated with

increases in tracer injection by overshooting parcels (their model cannot produce mean horizontal adiabatic temperature change at any vertical level because it has periodic lateral boundaries and a rigid lid). Sherwood et al. (2003) noted a cooled tropopause feature above convection in regional radiosonde data and inferred from a simple numerical model that this was likely caused by a combination of adiabatic ascent and diabatic turbulent mixing, and Robinson and Sherwood (2006) showed similar results using a cloud-resolving model.

### *b. Convective cold top in a linearized Boussinesq model*

To simulate the underlying process we believe is responsible for the ubiquity of the convective cold top, we use a simple linearized model of a uniformly stratified hydrostatic Boussinesq atmosphere initially at rest which is forced by constant sinusoidal heating and has a semi-infinite domain (as opposed to a rigid lid). The equations and parameters are discussed in detail in Nicholls et al. (1991), while a correction to the computational evaluation of the semi-infinite solutions, as well as a simpler equivalent solution for vertical velocity constructed by superimposing a series of pulse buoyancy sources at single levels, are presented by Pandya et al. (1993) [their Eq. (6)].

The basic linearized 2D equations (neglecting rotation) are:

$$\frac{\partial u}{\partial t} + \frac{1}{\rho_0} \frac{\partial p'}{\partial x} = 0 \quad (1)$$

$$\frac{1}{\rho_0} \frac{\partial p'}{\partial z} = b \quad (2)$$

$$\frac{\partial b}{\partial t} + wN^2 = Q \quad (3)$$

$$\frac{\partial u}{\partial x} + \frac{\partial w}{\partial z} = 0, \quad (4)$$

where  $u$ ,  $w$ ,  $p'$ ,  $b$ , and  $N$  are the horizontal velocity, vertical velocity, perturbation pressure, buoyancy, and buoyancy frequency per mass unit, respectively, and  $Q$  is the thermal forcing (Nicholls et al. 1991). Following Pandya et al. (1993) and Nicholls et al. (1991),  $\rho_0 = 1 \text{ kg m}^{-3}$ ,  $N = 0.01 \text{ s}^{-1}$ , and  $Q$  is constant in time, a heating rate that is sinusoidal in vertical height (only one positive heating mode, maximum at 5 km and going to zero at the surface and at 10 km) with a half-width in the horizontal at  $x = 10 \text{ km}$  and a magnitude  $Q_{m0} = 2.0 \text{ J kg}^{-1}$ . Vertical velocity ( $w$ ) is calculated analytically at each time step using Eq. (6) from Pandya et al. (1993). Buoyancy ( $b$ ) is determined by numerically integrating

Eq. (3) in time. To compare with our previous analysis, perturbation temperature  $T' = b/(\alpha g)$ , where  $\alpha$  is a linear thermal expansion coefficient such that  $\rho' = -\alpha \rho_0 T'$  and  $g$  is the gravitational constant. In an isothermal basic state approximation,  $\alpha = 1/T_0$ .

Figures 8a–b show the progression in time over two hours of  $w$  and  $b$  at  $x = 0$ . At early times,  $w$  quickly increases in a deep layer. Then, above the heating,  $w$  rapidly diminishes back toward zero, and steady state is reached with a warm troposphere and the cold top above. Figure 8c shows profiles of  $b$  after two hours of simulation for the center of the heating,  $x = 0$  (solid black line), and for a remote location with virtually no heating,  $x = 100$  km (grey dashed line). The two  $b$  profiles after two hours are nearly the same below the top of the heating, exhibiting the well-known behavior of gravity waves reducing horizontal gradients. The convective cold top is visible in both cases, although at  $x = 0$  the cold top is sharper and the maximum cooling occurs exactly at  $z = 10$  km, the lowest height, and thus the level with maximum  $w$  integrated in time, that has zero diabatic heating. The lower peak magnitude and more vertically-spread cold top at  $x = 100$  km is due to the effects of vertically propagating gravity waves which are now further from their source. Note that the higher (in altitude) level of the cold top minimum temperature away from the heating looks more like the observations in Figs. 2–7. At two hours time,  $b$  and  $w$  can be seen over many values of  $x$  in Fig. 1 of Pandya et al. (1993), including a convective cold top feature. A similar simulation (not shown) including both the half sine wave and an equal magnitude full sine wave, with heating in the upper half and cooling in the lower half of the troposphere (as in Nicholls et al. 1991), did not qualitatively change the cold top feature.

In Figs. 9a–c, a profile of  $w$  is plotted at three different times at  $x = 0$  (solid black line), and the constant  $Q/N^2$  value is shown in grey, with  $Q = 0$  above 10 km. Figures 9d–f show  $b$  at the same three times in solid black, along with  $p'$  in grey. Pressure is found by vertically integrating  $b$  using the hydrostatic equation (2), with the constant of integration set by the constraint that  $\int p'dz = 0$  (which holds if flow vanishes at some  $x$ ). We approximate this condition by extending the integration to 500 km and enforcing zero vertical mean, verifying that  $p'$  approaches zero at the top.

Hydrostatic pressure perturbations created by positive  $b$  in the troposphere must be compensated by  $p'$  above to satisfy  $\int p'dz = 0$ . At 0.04 hr (Fig. 9d) the troposphere has warmed significantly, but only small amplitude negative  $b$  has developed aloft at any given level. The  $p'$  above the heating thus decays very slowly with height, accelerating a very deep horizontal divergence. This produces positive  $w$  decaying only slowly above the heating (Fig. 9a). There is resulting adiabatic cooling where  $w$  is larger than  $Q/N^2$  and

warming where  $w$  is smaller, via Eq. (3). As negative  $b$  develops above the heating, where  $Q = 0$  and  $\partial b/\partial t = -wN^2$ , the magnitude of  $p'$  (and thus the magnitudes of  $b$  and  $w$ ) can decay more rapidly with height (Figs. 9b–c and 9e–f). This leads to a cold top increasingly concentrated around  $z = 10$  km (Figs. 9e–f), where there is maximum  $w$  above the heating function. At 0.40 hr  $w$  is approaching  $Q/N^2$  (Fig. 9c). By 2 hr,  $w$  is virtually equal to  $Q/N^2$  at all levels, and  $b$  reaches a steady state as shown in Fig. 8c. The convective cold top in this model thus arises entirely through adiabatic cooling near the top of and above the heating region.

The convective cold top as seen in Figs. 8–9 should not be thought of as parcels overshooting their levels of neutral buoyancy due to momentum conservation, since this is a hydrostatic model. Instead, horizontal pressure gradients extend above the top of the heating, creating divergence and broad ascent to satisfy continuity. Positive vertical velocity above the heating causes adiabatic cooling, which then reverses the sign of the left-hand side of Eq. (2), allowing pressure gradients to become very small aloft. The cold top takes longer to develop further from the heating, but after a short time the resulting  $b$  profiles look relatively similar.

### *c. A simple convective cold top explanation*

The above model experiment demonstrates the basic mechanism which we believe to be the fundamental cause of the convective cold top. In order for baroclinic pressure gradients generated by convective heating to become small at high altitudes, there must be cooling above the heating. In this simple hydrostatic model, the only mechanism available for this cooling is adiabatic, caused by horizontal divergence and broad vertical velocity reaching above the top of the heating. In the real atmosphere, diabatic cooling due to overshooting cumulus turrets or cloud-top radiation could contribute to part of the necessary cooling, but this would only result in smaller horizontal pressure gradients, less divergence, and less additional adiabatic cooling required to yield the same end result. Note that in the model, the response above the heating spreads to remote regions as fast as the tropospheric warming, a result not expected from local diabatic cooling alone.

To demonstrate quantitatively how temperature perturbations above convective heating relate to free tropospheric temperature perturbations in the data, we use the hydrostatic equation in pressure coordinates:

$$\Phi'(p) \approx R_d \int_p^{p_s} T'(p) d \ln p + \Phi'_s, \quad (5)$$

where  $\Phi'$  is the perturbation geopotential,  $R_d$  is the gas constant for dry air,  $p$  is the pressure,  $p_s$  is the surface pressure,  $T'$  is the perturbation temperature, and  $\Phi'_s$  is the surface geopotential perturbation. This result, applied to the temperature regression slopes shown earlier in Figs. 2–6, gives the geopotential perturbation profile associated with one degree of free tropospheric vertically averaged warming. Because there is a barotropic as well as a baroclinic component to  $\Phi'_s$ , we then subtract the vertical mean of this profile,  $\hat{\Phi}'$ , since  $[\Phi' - \hat{\Phi}']$  is independent of  $\Phi'_s$ , with  $\hat{\Phi}'$  defined as follows:

$$\hat{\Phi}' = \left( \frac{1}{p_s - p_t} \right) \int_{p_t}^{p_s} \Phi'(p) dp, \quad (6)$$

where  $p_t$  is the pressure at the top of the available atmospheric data. This represents baroclinic geopotential perturbations if the barotropic mode is separated from the baroclinic mode (e.g. surface drag effects and vertical shear effects are minimal). To the extent that these two modes are instead interacting, the actual  $\Phi'$  will be shifted by a vertical constant from the results shown here.

Figure 10 shows six plots of  $[\Phi' - \hat{\Phi}']$ , indicating that at most scales the convective cold top brings down the baroclinic pressure gradients significantly relative to their peak values. The  $d \ln p$  differential in Eq. (5) implies that temperature anomalies at upper levels are especially effective at contributing to net geopotential gradients near the top of the atmosphere. We have included regression coefficients at all available pressure levels, including those that are not statistically significant at the 95% level, since we have no other values to use. The "zero wind" level occurs uniformly near 400 hPa. Figure 10a suggests that at large scales cold top effects are not as strong, but this smaller cold top may be due to the QBO signal. In contrast, Fig. 10c shows a stronger-than-expected cold top for monthly AIRS data in the western Pacific. Figure 10b over a similar region for monthly CARDS data shows an expected cold top magnitude, along with daily analyses in the Pacific warm pool region for three different datasets (Figs. 10d–f).

To summarize, combining the analysis above with interpretation from the simple model: a cold top layer is necessary above a warmed troposphere to reduce pressure gradients above the heating. Unless diabatic cooling of sufficient magnitude happens to occur, the circulation due to pressure gradients will tend to yield adiabatic cooling, producing the needed cold top.

## 6. Summary and discussion

The majority of analyses over various datasets, time scales, and space scales show that temperature perturbation regressions at different pressure levels can be divided into three main features: the boundary layer, a highly coherent free troposphere, and the convective cold top above, with a minimum negative correlation near or above the tropopause. These three primary features are evident even when temperatures at individual levels are regressed on temperature averaged over the entire column, or on temperatures at individual levels within the free troposphere (not shown), instead of on a free tropospheric average. Figure 11 is a schematic illustrating these vertical features, using the CARDS analysis from Fig. 4. A brief discussion of each feature and some of its implications follows below.

### a. Coherent free troposphere

The free troposphere, from about 800–200 hPa, is the layer with the highest correlation coefficients when temperature at each level is regressed on the free tropospheric vertical average temperature. These free tropospheric temperature perturbations are similar to those derived from an ensemble of moist adiabats with surface conditions typical of warm tropical oceans. Some deviations from the moist-adiabatic curve, especially for AIRS satellite data, may be due to places and times that are not strongly convecting (such as the region shown in Fig. 7), or to freezing/melting processes, although this remains a topic for future research. The coherence of the free troposphere tends to decrease at smaller scales, but more so for NCEP reanalysis than for other observational data.

Overall, the highly coherent free troposphere is consistent with expectations from theory: namely, QE establishes a coherent vertical mean temperature structure in convective zones and then gravity waves quickly spread this signal over large scales. These results are much more consistent with QE expectations than other approaches that have analyzed relationships between the free troposphere and the boundary layer. This high coherence can be utilized to predict baroclinic pressure gradients and winds using simplified vertical temperature structures.

### b. Independent boundary layer

Below the free troposphere is a largely independent boundary layer, from about 1000–850 hPa. For typical tropical ocean conditions this reaches above the LCL, which is between 925 and 900 hPa. The boundary layer

generally has a correlation with the free troposphere on the order of 0.5 or less even at monthly time scales and large space scales, and smaller for smaller scales, with regression coefficients usually below those of the moist-adiabatic ensemble. The boundary layer temperature in NCEP tends to covary highly with the free troposphere to a greater extent than in AIRS and radiosonde data. This suggests that convective parameterizations may misrepresent the troposphere-boundary layer temperature relationship, even while correctly capturing the temperature perturbation profile in the free troposphere. Preliminary analyses of global climate model (GCM) output and ERA-40 reanalysis (not shown) give results similar to NCEP.

One important reason for a distinctive boundary layer is that we are only regressing temperature on temperature, rather than a measure of boundary layer moist static energy such as  $\theta_e$ , since we are primarily interested in the vertical coherence of temperature signals and corresponding pressure gradients. It is possible that boundary layer  $\theta_e$  might track that of the free troposphere, if changes in boundary layer relative humidity compensate for variations in boundary layer temperature. However, based on studies such as Brown and Bretherton (1997), which did use  $\theta_e$  in the boundary layer, and a few similar tests we did using NCEP and CARDS data, it is not that simple. Another likely explanation is that the free troposphere is more homogeneous, constantly modified by fast-moving gravity waves from various sources of deep convection, especially over the warmest ocean surfaces. The boundary layer should have more influence from local surface fluxes. The relationship to convective heating is complicated at smaller scales by subsaturated downdrafts which reduce boundary layer  $\theta_e$  (Cheng 1989). Finally, when convection is locally suppressed, for instance by a lack of conditional instability or by dry air infusions above the boundary layer, QE no longer applies and there is little reason for temperature to behave coherently through the whole troposphere. Likely, all of these effects and possibly others are working simultaneously, and the boundary layer will be a topic of future work.

### *c. Convective cold top*

A nearly universal finding is a statistically significant negative correlation coefficient (between temperature and free tropospheric average temperature) somewhere from about 100–50 hPa depending on the dataset. We refer to this phenomenon as the “convective cold top.” We find it at many different scales. It is unlikely that the negative correlations seen here on long time scales are related to climate change (i.e. greenhouse gas warming in the troposphere

correlating with greenhouse gas cooling in the stratosphere) because we find little trend in free tropospheric temperatures over the years analyzed for NCEP reanalysis and the relatively few years with available stratospheric temperatures for CARDS.

Using a linearized Boussinesq model with constant heating, we illustrate a simple explanation for this feature. We show that as gravity waves spread the warming due to convective heating through the free troposphere, hydrostatic pressure gradients will extend above the heating, causing divergence, ascent, and adiabatic cooling aloft. This extension of outflow above the top of the heating has important implications for calculations of gross moist stability, which have been shown to be sensitive to the top level of integration (Yu et al. 1998).

In the real atmosphere, cooling by some means is necessary above areas of heating in order for hydrostatic pressure gradients to become small at high altitudes. Therefore, any diabatic cooling associated with convective heating should only reduce the amount of adiabatic cooling required by our proposed mechanism. If these horizontal pressure gradients did not go to zero above convective heating, they would cause anomalous divergence and adiabatic cooling, which would then reduce them. The convective cold top should be thought of as an intrinsic response to convective heating, and as an inherent part of quasi-equilibrium temperature adjustment.

*Acknowledgments.* We thank J. E. Meyerson for graphical assistance and D. Durran, E. Fetzer, E. Olsen, B. Khan, S. Bordoni, B. Medeiros, V. Savic-Jovcic, N. Lovenduski, G. Mullendore, and B. Stevens for helpful discussions. CSU data were obtained from the R. Johnson Research Group web page. Many thanks to the AIRS project at NASA JPL, NCEP/NCAR, and the CARDS project for providing data. This work was supported under National Science Foundation Grant ATM-0082529, National Oceanic and Atmospheric Administration Grants NA05OAR4311134 and ATM-0645200, and NASA Earth System Science Fellowship Grant NNX06AF83H. This is IGPP contribution 6280.

## APPENDIX

### **Sensitivity of Moist Adiabats**

In order to demonstrate that moist-adiabatic regression coefficients show little variability over typical tropical precipitating conditions, we present an analysis of the original NCEP daily data (with no harmonics removed, and no spatial or temporal averaging) used in Fig. 2. We use temperatures and specific humidities between 15°S and 15°N, at 1000

hPa, for grid points with more than 2 mm day<sup>-1</sup> of precipitation. To facilitate analysis, 10% of these data (73,015 points) have been randomly selected. We produce (with the same code described in section 3) an array of reversible moist adiabats starting from each point. Figure A1 shows the temperatures at each level plotted against the 850–200 hPa column average temperatures for each calculated sounding. Pressure has been labeled for each data curve, on alternate sides. Diamonds along the horizontal axis mark the location of the distribution octiles (eighth quantiles, defining the boundaries between the eighths). Vertical average temperature correlates almost perfectly with 1000 hPa  $\theta_e$  (not shown), though the relationship is weakly nonlinear.  $\theta_e$  equals 348.5 K, 354.4 K, and 360.1 K at the first octile, median, and seventh octile, respectively. The lines in Fig. A1 are very linear above 925 hPa, especially within the center three quarters of the data, signifying little sensitivity of the slopes of moist-adiabatic temperature perturbations at these levels to 850–200 hPa column average moist adiabat temperature (and thus to 1000 hPa  $\theta_e$ ) for typical tropical values. The curvature increases slightly above 300 hPa as the transition to nearly dry adiabats occurs sooner for profiles with smaller vertical average temperature values.

Figure A2 shows the regression values in black from the data shown in Fig. A1 for three ranges: the first to second octiles, the third to fifth octiles, and the sixth to seventh octiles. The curves are nearly identical between 925 and 300 hPa. Above 300 hPa, curves with lower  $\theta_e$  values begin curving back towards a negative linear slope (characteristic of dry adiabats) faster, since they have less water vapor left at a given level. To generate the curve shown in Figs. 2–7, we used a 1000 hPa temperature range (298–301 K) and constant relative humidity (83%) close to the mean values of the analyzed NCEP data between the third and fifth octiles (299.8 K and 83.2%, respectively). This curve is shown as a dashed grey line, as in previous figures, and lies between the left and middle curves above 300 hPa. Note that even an analysis using 1000 hPa ranges far from typical tropical precipitating values (292–295 K, and 304–307 K, with 75% and 90% relative humidity, respectively) show a maximum difference in regression coefficients with the curve shown in Figs. 2–7 of only 0.09 between 1000 and 300 hPa.

## REFERENCES

- Arakawa, A., and W. H. Schubert, 1974: Interaction of a cumulus cloud ensemble with the large-scale environment, Part I. *J. Atmos. Sci.*, **31**, 674–701.
- Arakawa, A., 2004: The cumulus parameterization problem: past, present, and future. *J. Climate*, **17**, 2493–2525.
- Arakawa, H., 1950: Analysis of the tropopause and the stratospheric field of temperature of a mature typhoon. *Pap. Meteorol. Geophys.*, **2**, 1–5.
- Betts, A. K., 1973: Non-precipitating cumulus convection and its parameterization. *Quart. J. R. Met. Soc.*, **99**, 178–196.
- Betts, A. K., and M. J. Miller, 1986: A new convective adjustment scheme. Part II: Single column tests using GATE wave, BOMEX, ATEX and arctic air-mass data sets. *Quart. J. Roy. Meteor. Soc.*, **112**, 693–709.
- Bretherton, C. S., M. Widmann, V. Dymnikov, J. Wallace, and I. Bladé, 1999: The effective number of spatial degrees of freedom of a time-varying field. *J. Climate*, **12**, 1990–2009.
- Brown, R. G., and C. S. Bretherton, 1997: A test of the strict quasi-equilibrium theory on long time and space scales. *J. Atmos. Sci.*, **54**, 624–638.
- Cheng, M.-D., 1989: Effects of downdrafts and mesoscale convective organization on the heat and moisture budgets of tropical cloud clusters. Part II: Effects of convective-scale downdrafts. *J. Atmos. Sci.*, **46**, 1540–1565.
- Chiang, J. C. H., and A. H. Sobel, 2002: Tropical tropospheric temperature variations caused by ENSO and their influence on the remote tropical climate. *J. Climate*, **15**, 2616–2631.
- Ciesielski, P. E., L. Hartten, and R. H. Johnson, 1997: Impacts of merging profiler and rawinsonde winds on TOGA COARE analyses, *J. of Atmos. and Oceanic Tech.*, **14**, 1264–1279.
- Ciesielski, P. E., R. H. Johnson, P. T. Haertel, and J. Wang, 2003: Corrected TOGA COARE sounding humidity data: Impact on diagnosed properties of convection and climate over the warm pool. *J. Climate*, **16**, 2370–2384.
- Collimore, C. C., D. W. Martin, M. H. Hitchman, A. Huesmann, and D. E. Waliser, 2003: On the relationship between the QBO and tropical deep convection. *J. Climate*, **16**, 2552–2568.
- Danielsen, E. F., 1993: In situ evidence of rapid, vertical, irreversible transport of lower tropospheric air into the lower tropical stratosphere by convective cloud turrets and by larger-scale upwelling in tropical cyclones. *J. Geophys. Res.*, **98**, 8665–8681.
- Divakarla, M., C. Barnet, M. D. Goldberg, L. McMillin, E. S. Maddy, W. W. Wolf, L. Zhou, and X. Liu, 2006: Validation of Atmospheric Infrared Sounder temperature and water vapor retrievals with matched radiosonde measurements and forecasts. *J. Geophys. Res.*, 111D, doi:10.1029/2005JD006116.
- Durre, I., R. S. Vose, and D. B. Wuertz, 2006: Overview of the Integrated Global Radiosonde Archive. *J. Climate*, **19**, 53–68.
- Emanuel, K., 1991: A scheme for representing cumulus convection in large-scale models. *J. Atmos. Sci.*, **48**, 2313–2335.
- Emanuel, K. A., 1994: *Atmospheric Convection*. Oxford University Press, 580 pp.
- Eskridge, R. E., O. A. Alduchov, I. V. Chernykh, Z. Panmao, A. C. Polansky, and S. R. Doty, 1995: A Comprehensive Aerological Reference Data Set (CARDS): Rough and systematic errors. *Bull. Amer. Meteor. Soc.*, **76**: 1759–1775.

- Fritsch, J. M., and J. M. Brown, 1982: On the generation of convectively driven mesohighs aloft. *Mon. Wea. Rev.*, **110**, 1554–1563.
- Gill, A. E., 1980: Some simple solutions for heat-induced tropical circulation. *Quart. J. Roy. Meteor. Soc.*, **106**, 447–462.
- Haertel, P. T., and G. N. Kiladis, 2004: Dynamics of 2-day equatorial waves. *J. Atmos. Sci.*, **61**, 2707–2721.
- Highwood, E. J., and B. J. Hoskins, 1998: The tropical tropopause. *Quart. J. Roy. Meteor. Soc.*, **124**, 1579–1604.
- Holton, J. R., and A. Gettelman, 2001: Horizontal transport and the dehydration of the stratosphere. *Geophys. Res. Lett.*, **28**, 2799–2802.
- Huesmann, A. S., and M. H. Hitchman, 2001: The stratospheric quasi-biennial oscillation in the NCEP reanalyses: Climatological structures. *J. Geophys. Res.*, **106**, 11859–11874.
- Johnson, R. H., and D. C. Kriete, 1982: Thermodynamic and circulation characteristics of winter monsoon tropical mesoscale convection. *Mon. Wea. Rev.*, **110**, 1898–1911.
- Jordan, C. L., 1960: Abnormally cold tropopause temperatures in the equatorial Pacific. *Mon. Wea. Rev.*, **88**, 151–154.
- Kalnay, E., and Coauthors, 1996: The NCEP/NCAR 40-year reanalysis project. *Bull. Amer. Meteor. Soc.*, **77**, 437–471.
- Koteswaram, P., 1967: On the structure of hurricanes in the upper troposphere and lower stratosphere. *Mon. Wea. Rev.*, **95**, 541–564.
- Kuang, Z., and C. S. Bretherton, 2004: Convective influence on the heat balance of the tropical tropopause layer: A cloud-resolving model study. *J. Atmos. Sci.*, **61**, 2919–2927.
- Manabe, S., J. Smagorinsky, and R. F. Strickler, 1965: Simulated climatology of a general circulation model with a hydrologic cycle. *Mon. Wea. Rev.*, **93**, 769–798.
- Moorthi, S., and M. J. Suarez, 1992: Relaxed Arakawa-Schubert: A parameterization of moist convection for general circulation models. *Mon. Wea. Rev.*, **120**: 978–1002.
- Neelin, J. D., 1997: Implications of convective quasi-equilibrium for the large-scale flow. *The Physics and Parameterization of Moist Atmospheric Convection*, R. K. Smith, Ed., Kluwer Academic Publishers, 413–446.
- Neelin, J. D., and N. Zeng, 2000: A quasi-equilibrium tropical circulation model—Formulation. *J. Atmos. Sci.*, **57**, 1741–1766.
- Nicholls, M. E., R. A. Pielke, and R. W. Cotton, 1991: Thermally forced gravity waves in an atmosphere at rest. *J. Atmos. Sci.*, **48**, 1869–1884.
- Pan, H., and W. Wu, 1995: Implementing a mass flux convection parameterization from package for the NMC medium-range forecast model. NOAA/NMC/NCEP Office Note 409, 43 pp.
- Pandya, R., D. Durran, and C. Bretherton, 1993: Comments on “Thermally forced gravity waves in an atmosphere at rest”. *J. Atmos. Sci.*, **50**, 4097–4101.
- Pandya, R. E., and D. R. Durran, 1996: The influence of convectively generated thermal forcing on the mesoscale circulation around squall lines. *J. Atmos. Sci.*, **53**, 2924–2951.
- Plumb, R. A., and R. C. Bell, 1982: A model of the quasi-biennial oscillation on an equatorial beta-plane. *Quart. J. Roy. Meteor. Soc.*, **108**, 335–352.
- Randall, D. A., and D. M. Pan, 1993: Implementation of the Arakawa-Schubert cumulus parameterization with a prognostic closure. *Bull. Amer. Meteor. Soc.*, **74**, 137–144.
- Raymond, D. J., 1997: Boundary layer quasi-equilibrium (BLQ). *The Physics and Parameterization of Moist Atmospheric Convection*, R. K. Smith, Ed., Kluwer Academic Publishers, 387–397.
- Reid, G. C., 1994: Seasonal and interannual temperature variations in the tropical stratosphere. *J. Geophys. Res.*, **99D**, 18923–18932.
- Reid, G. C., and K. S. Gage, 1996: The tropical tropopause over the western Pacific: Wave driving, convection, and the annual cycle. *J. Geophys. Res.*, **101D**, 21233–21241.
- Reid, G. C., K. S. Gage, and J. R. McAfee, 1989: The thermal response of the tropical atmosphere to variations in equatorial Pacific sea surface temperature. *J. Geophys. Res.*, **94D**, 14705–14716.
- Robinson, F. J., and S. C. Sherwood, 2006: Modeling the impact of convective entrainment on the tropical tropopause. *J. Atmos. Sci.*, **63**, 1013–1027.
- Sherwood, S. C., T. Horinouchi, and H. A. Zeleznik, 2003: Convective impact on temperatures observed near the tropical tropopause. *J. Atmos. Sci.*, **60**, 1847–1856.
- Sobel, A. H., S. E. Yuter, C. S. Bretherton, and G. N. Kiladis, 2004: Large-scale meteorology and deep convection during TRMM KWAJEX. *Mon. Wea. Rev.*, **132**, 422–444.
- Susskind, J., C. D. Barnett, and J. M. Blaisdell, 2003: Retrieval of atmospheric and surface parameters from AIRS/AMSU/HSB data in the presence of clouds. *IEEE Trans. Geosci. Remote Sensing*, **41**, 390–409.
- Teitelbaum, H., M. Moustou, C. Basdevant, and J. R. Holton, 2000: An alternative mechanism explaining the hygropause formation in tropical region. *Geophys. Res. Lett.*, **27**, 221–224.
- Thuburn, J., and G. C. Craig, 2002: On the temperature structure of the tropical stratosphere. *J. Geophys. Res.*, **107D**, 4017, doi:10.1029/2001JD000448.
- Tobin, D.C., H. E. Revercomb, R. O. Knuteson, B. Lesht, L. L. Strow, S. E. Hannon, W. F. Feltz, L. Moy, E. J. Fetzer, and T. Cress, 2006: Atmospheric Radiation Measurement site atmospheric state best estimates for Atmospheric Infrared Sounder temperature and water vapor retrieval validation. *J. Geophys. Res.*, **111D**, doi:10.1029/2005JD006103.
- Trenberth, K. E., and L. Smith, 2006: The vertical structure of temperature in the tropics: Different flavors of El Niño. *J. Climate*, in press.
- Webster, P. J., and G. L. Stephens, 1980: Tropical upper-tropospheric extended clouds: Inferences from Winter MONEX. *J. Atmos. Sci.*, **37**, 1521–1541.
- Xu, K., and K. A. Emanuel, 1989: Is the tropical atmosphere conditionally unstable? *Mon. Wea. Rev.*, **117**, 1471–1479.
- Yu, J.-Y., C. Chou, and J. D. Neelin, 1998: Estimating the gross moist stability of the tropical atmosphere. *J. Atmos. Sci.*, **55**, 1354–1372.

Zhang, G. J., and N. A. McFarlane, 1995: Sensitivity of climate simulations to the parameterization of cumulus convection in the Canadian Climate Centre general circulation model. *Atmos.-Ocean.*, **33**, 407–446.

## Figures

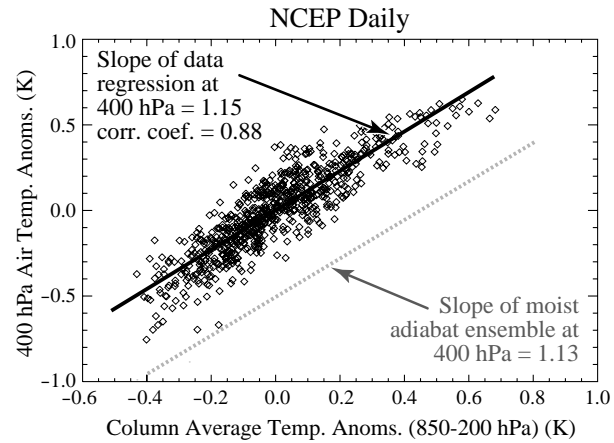


FIG. 1. Schematic showing our method of regression analysis, for NCEP reanalysis temperature anomalies, November 2003–November 2005, 15°S–15°N. The slope of each line will be represented in subsequent figures by single regression coefficient values at that pressure level, with the correlation coefficient on another, similar plot.

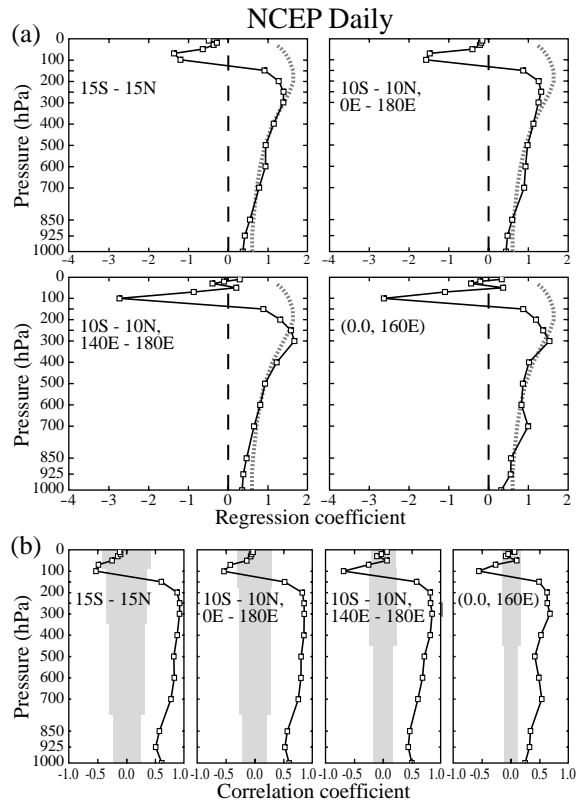


FIG. 2. NCEP November 2003–November 2005 daily anomalies (with three harmonics of the seasonal cycle, and a two-year harmonic, removed) for four tropical boxes. (a) Regression coefficients (squares) with moist-adiabatic curve (dashed grey line). (b) Correlation coefficients with grey shading between the critical values for 95% significance.

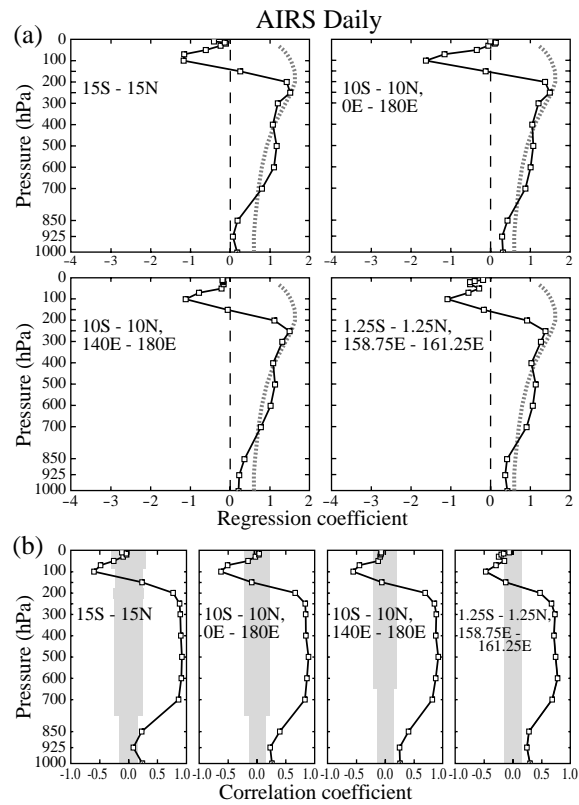


FIG. 3. AIRS daily anomalies over ocean for the same four tropical boxes as in Fig. 2. (a) Regression coefficients (squares) with moist-adiabatic curve (dashed grey line). (b) Correlation coefficients with grey shading between the critical values for 95% significance.

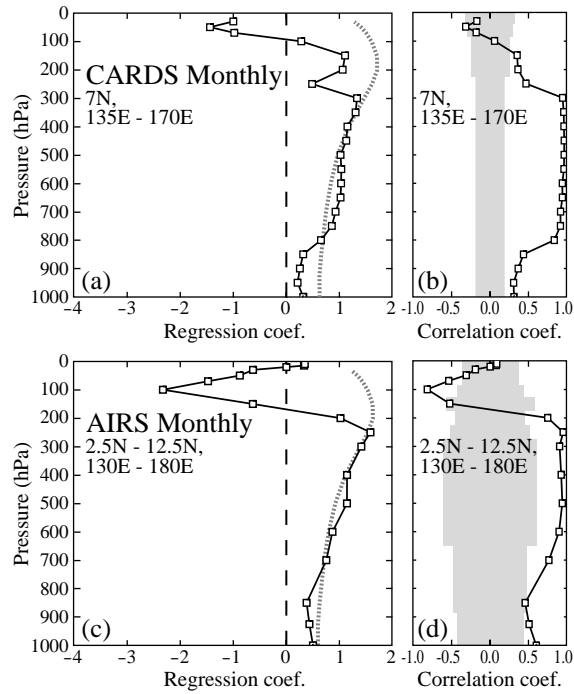


FIG. 4. CARDS 1953–1999, monthly anomalies for an average over three radiosonde stations on tropical western Pacific islands, and AIRS monthly anomalies from two years of daily anomalies. (a) and (c) Regression coefficients (squares) with moist-adiabatic curve (dashed grey line). (b) and (d) Correlation coefficients with grey shading between the critical values for 95% significance. Note that y-axis labels for both datasets and vertical sampling for CARDS are slightly different from other data analysis figures.

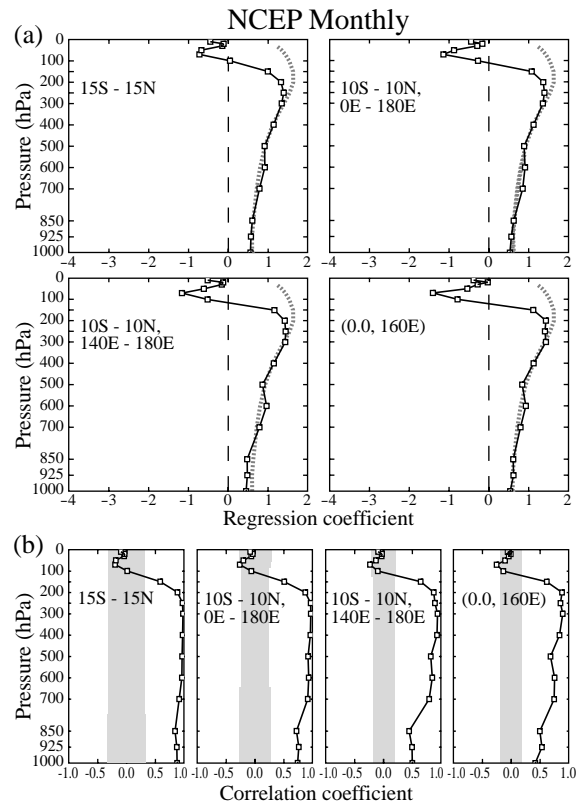


FIG. 5. NCEP 1979–2003 monthly anomalies for the same four tropical boxes as in Fig. 2. (a) Regression coefficients (squares) with moist-adiabatic curve (dashed grey line). (b) Correlation coefficients with grey shading between the critical values for 95% significance.



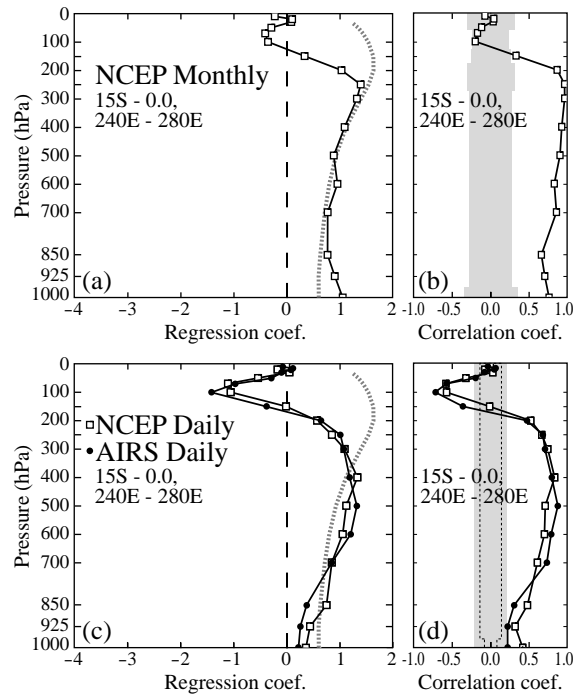


FIG. 7. An eastern Pacific, largely non-convecting region. (a) Regression coefficients for NCEP monthly anomalies (squares) with moist-adiabatic curve (dashed grey line). (b) Correlation coefficients for NCEP monthly anomalies with grey shading between the critical values for 95% significance. (c) Regression coefficients for NCEP daily anomalies (open squares) and AIRS daily anomalies (filled circles) with moist-adiabatic curve (dashed grey line). (d) Correlation coefficients for NCEP daily anomalies (open squares) and AIRS daily anomalies (filled circles). Critical values for 95% significance are shown by grey shading (NCEP) or dashed lines (AIRS).

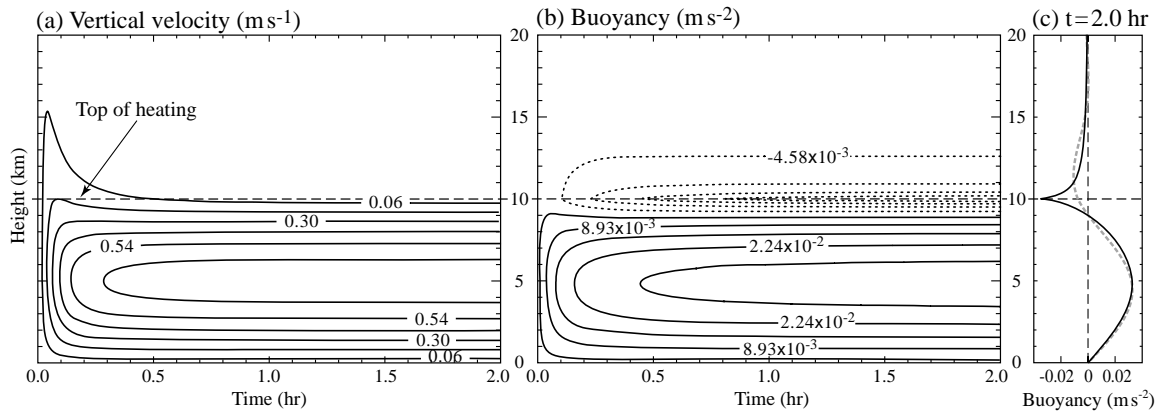


FIG. 8. Linear Boussinesq model: (a)  $w$  in  $\text{m s}^{-1}$  at  $x = 0$ ; (b)  $b$  in  $\text{m s}^{-2}$  at  $x = 0$ , dotted contours are negative; (c)  $b$  profile at  $t = 2$  hr for  $x = 0$  (solid black line) and  $x = 100$  km (dashed grey line). The buoyancy ( $b$ ) is proportional to  $T'$ .

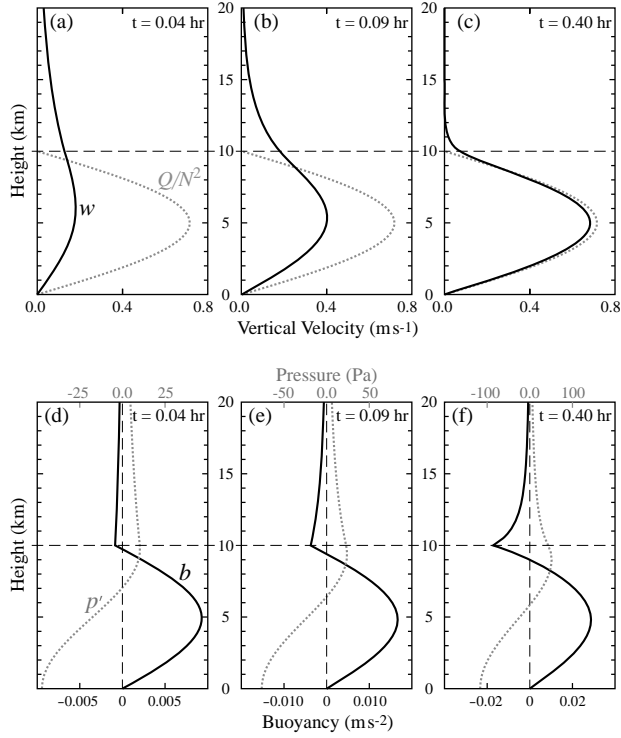


FIG. 9. Linear Boussinesq model at  $x = 0$ : (a–c)  $w$  in  $\text{m s}^{-1}$  (solid black line) and  $Q/N^2$  (dashed grey line, same units) at three times; (d–f)  $b$  in  $\text{m s}^{-2}$  (solid black line) and  $p'$  in Pa (dashed grey line). Note that x-axes for  $b$  and  $p'$  double in scale from (d) to (e), and again from (e) to (f).

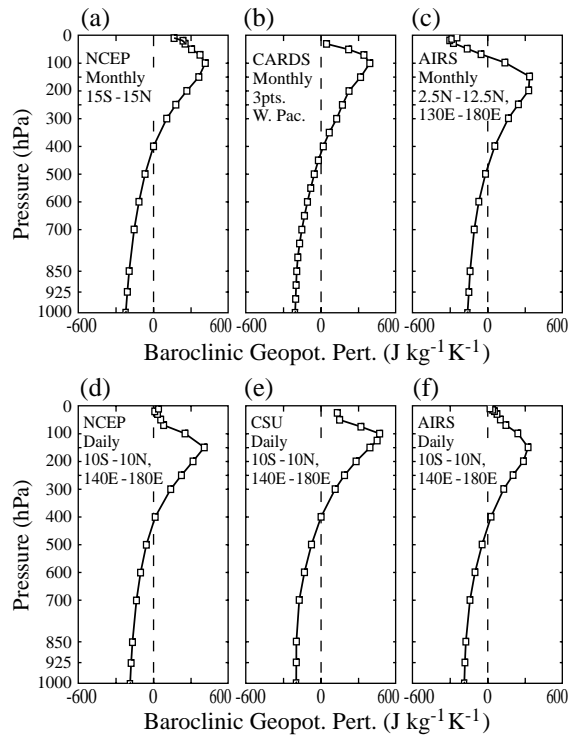


FIG. 10. Baroclinic geopotential perturbations per vertical average temperature perturbation with vertical average removed,  $[\Phi' - \hat{\Phi}']$ , calculated using the hydrostatic equation (5). (a) NCEP reanalysis 1979–2003 monthly anomalies. (b) CARDS 1953–1999 monthly anomalies. (c) AIRS Monthly Nov. 2003–2005 anomalies. (d) NCEP Nov. 2003–2005 daily averages with three harmonics of the seasonal cycle removed. (e) CSU TOGA COARE November 1992–February 1993 daily averages. (f) AIRS Daily Nov. 2003–2005 anomalies. Horizontal boxes labeled on panels.

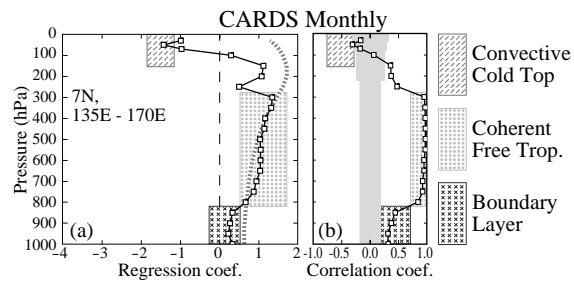


FIG. 11. Schematic of the three main features of the vertical temperature structure, illustrated for the CARDS monthly anomalies (Regression and correlation coefficients) from Fig. 4.

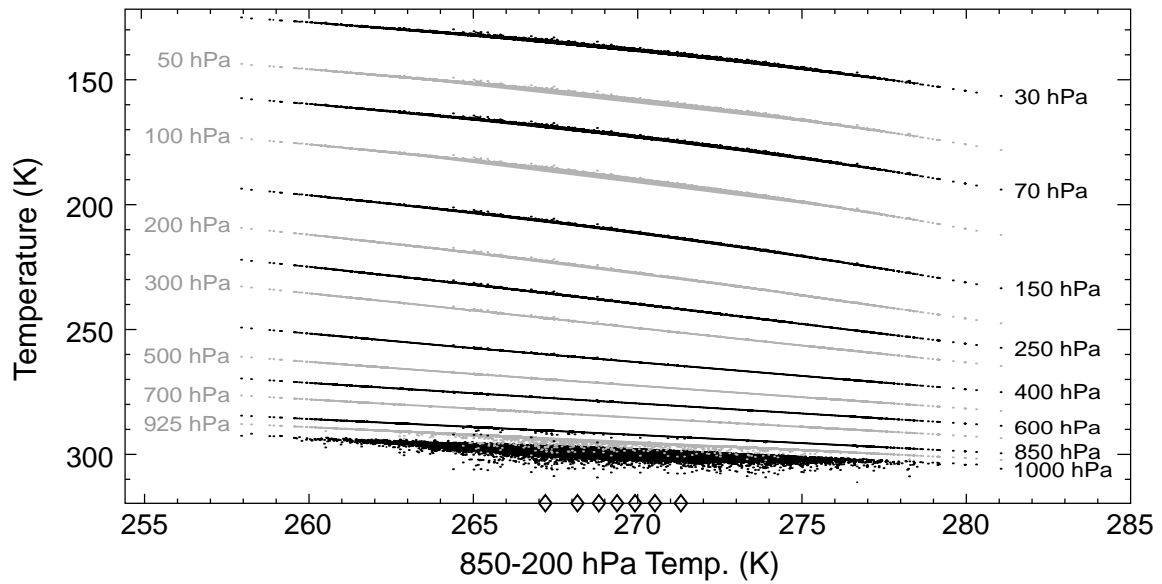


FIG. A1. Temperature of reversible moist adiabats calculated from 1000 hPa NCEP daily temperature and humidity data, Nov. 2003–2005, for grid points between 15°S and 15°N, masked for precipitation greater than 2 mm day<sup>-1</sup>. Note that the vertical axis is temperature increasing downward. The horizontal axis is the 850–200 hPa column average temperature of each moist adiabat profile. Pressure levels are labeled alternately at right and left for each data curve. The position of the distribution octiles (eighth quantiles) of column average temperature are represented with diamonds on the horizontal axis.

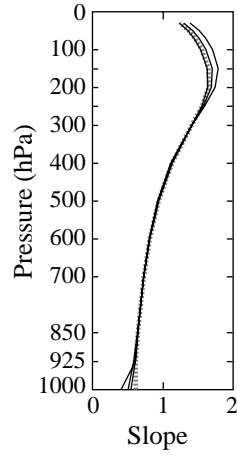


FIG. A2. Regression coefficients (black lines) of reversible moist adiabats in Fig. A1, for data lying between the first and second octiles, third and fifth octiles, and sixth and seventh octiles, respectively (curves appear in this order at upper levels). The grey dashed line is the curve used in Figs. 2–7, with the same aspect ratio as in those figures.